ARTICLE

The Anatomical Record
Advances in Integrative Anatomy and Evolutionary Biology

WILEY

Humerus osteology, myology, and finite element structure analysis of Cheloniidae

Anna Krahl[1] ⬤ | Andreas Lipphaus[1] | Martin P. Sander[2] | Fulvio Maffucci[3] |
Sandra Hochscheid[4] | Ulrich Witzel[1]

[1]Biomechanics Research Group, Lehrstuhl für Produktentwicklung, Faculty of Mechanical Engineering, Ruhr-University Bochum, Bochum, Germany

[2]Institute of Geosciences, Division of Paleontology, University of Bonn, Bonn, Germany

[3]Research Infrastructures for Marine Biological Resources, Stazione Zoologica Anton Dohrn, Naples, Italy

[4]Marine Turtle Research Center, Stazione Zoologica Anton Dohrn, Portici, Italy

Correspondence

Anna Krahl, Biomechanics Research Group, Lehrstuhl für Produktentwicklung, Faculty of Mechanical Engineering, Ruhr-University Bochum, Universitätsstr. 150, Building IC1-163, 44801 Bochum, Germany.
Email: anna.krahl@rub.de

Funding information

Deutsche Forschungsgemeinschaft, Grant/Award Number: WI1389/8-1

Abstract

Adaptation of osteology and myology lead to the formation of hydrofoil fore-flippers in Cheloniidae (all recent sea turtles except *Dermochelys coriacea*) which are used mainly for underwater flight. Recent research shows the biomechanical advantages of a complex system of agonistic and antagonistic tension chords that reduce bending stress in bones. Finite element structure analysis (FESA) of a cheloniid humerus is used to provide a better understanding of morphology and microanatomy and to link these with the main flipper function, underwater flight. Dissection of a *Caretta caretta* gave insights into lines of action, that is, the course that a muscle takes between its origin and insertion, of foreflipper musculature. Lines of action were determined by spanning physical threads on a skeleton of *Chelonia mydas*. The right humerus of this skeleton was micro-CT scanned. Based on the scans, a finite element (FE) model was built and muscle force vectors were entered. Muscle forces were iteratively approximated until a uniform compressive stress distribution was attained. Two load cases, downstroke and upstroke, were computed. We found that muscle wrappings (m. coracobrachialis magnus and brevis, several extensors, humeral head of m. triceps) are crucial in addition to axial loading to obtain homogenous compressive loading in all bone cross-sections. Detailed knowledge on muscle disposition leads to compressive stress distribution in the FE model which corresponds with the bone microstructure. The FE analysis of the cheloniid humerus shows that bone may be loaded mainly by compression if the bending moments are minimized.

KEYWORDS

Cheloniidae, dissection, FESA, humerus, lines of action, micro-CT, muscle forces

1 | INTRODUCTION

1.1 | Foreflipper osteology and myology of Cheloniidae

In comparison to other Testudines, Cheloniidae display numerous osteological and myological adaptations especially in the pectoral girdle (Walker, 1971; Walker, 1973; Wyneken, 1997; Depecker, Berge, Penin, & Renous, 2006) and foreflippers (Renous, 1995; Rivera, Wyneken, & Blob, 2011; Walker & Westneat, 2000; Wyneken, 1997) which form hydrofoils (Davenport, Munks, & Oxford, 1984). Some locomotory muscle origins spread onto the carapace and plastron, that is, the musculus (m.) latissimus dorsi/teres major, m. pectoralis, and m. deltoideus clavicularis (Walker, 1973; Wyneken, 2001). The coracoid of Cheloniidae is relatively enlarged and shows large attachment areas for the m. biceps complex (i.e., m. brachialis inferior, m. biceps profundus, m. biceps superficialis) and m. coracobrachialis brevis (Walker, 1973; Depecker et al., 2006). The scapula is reduced in size, and the origin sites of m. latissimus dorsi/teres major, m. deltoideus scapularis, and m. subscapularis are relatively smaller (Walker, 1973) than in other turtles. Humeri of sea turtles, like long bones of other Tetrapoda, show in proximodistal section that they are hourglass-

FIGURE 1 Muscle attachment areas on (a) the ventral and (b) the dorsal sea turtle humerus as derived from *Caretta caretta* dissection. Attachment area for eri had to be inferred. bc, m. biceps complex (i.e., bi, brachialis inferior; bs, biceps superficialis; bp, biceps profundus); cb, m. coracobrachialis brevis; cm, m. coracobrachialis magnus; dc, m. deltoideus clavicularis; ds, m. deltoideus scapularis; ecu, m. extensor carpi ulnaris; ef, entepicondylar foramen; eri, m. extensor radialis intermedius; ers + edc, m. extensor radialis superficialis + m. extensor digitorum communis; fcr, m. flexor carpi radialis; fcu, m. flexor carpi ulnaris; ld/tm, m. latissimus dorsi/teres major; lh, lateral head; mh, medial head; p, m. pectoralis; pl, palmaris longus; pt, m. pronator teres; sc, m. supracoracoideus; ss, m. subscapularis; tb, m. triceps brachii; tr, m. tractor radii

shaped which reflects cones of endochondral bone surrounded by a mantle of periosteal bone (Francillon-Vieillot et al., 1990). The v-shaped lateral process provides insertion area for m. pectoralis and m. supracoraoideus (Walker, 1973; Hirayama, 1994; Wyneken, 2001; Figure 1). The greatly expanded proximal medial process on the sea turtle humerus hosts attachment surfaces for the hypertrophied m. coracobrachialis magnus and m. subscapularis (Figure 1). The ulna lies relatively dorsal and posterior to the markedly longer radius. The ulnare and intermedium are much larger than the radiale in turn. Connective tissue ontogenetically conjoins radius and ulna. The pisiform is enlarged. The flipper blade evolved by elongation of the phalanges of digit II, III, and IV (Walker, 1973; Wyneken, 2001). In sea turtles some extensors and flexors, especially in the manus, were reduced, but the remaining ones are well developed (Walker, 1973). Fusion of muscles, extensive formation of aponeuroses, and connective tissue partially fused to the dermis are responsible for the development of a semi-rigid flipper during postnatal ontogeny (Walker, 1973; Wyneken, 2001; Abdala, Manzano, & Herrel, 2008).

Adult Chelonioidea usually swim by underwater flight. In this mode of locomotion, the humerus is mainly moved through the vertical plane and subordinately through the horizontal plane (Davenport et al., 1984; Pace, Blob, & Westneat, 2001; Rivera et al., 2011; Rivera, Rivera, & Blob, 2013; Walker, 1971). During the downstroke, the humerus is depressed and retracted, the elbow flexed (Davenport et al., 1984; Rivera et al., 2011) and the anterior flipper edge is rotated downward. During the upstroke, the humerus is elevated and protracted, the elbow extended (Davenport et al., 1984; Rivera et al., 2011), and the anterior flipper edge is rotated upwards. Thus, the flipper tip describes the path of a skewed slim "O" in anterodorsal–posteroventral direction during underwater flight (Davenport et al., 1984; Rivera et al., 2011).
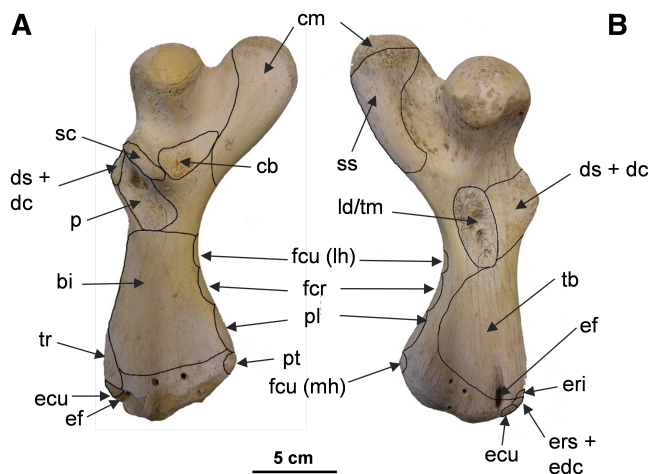
1.2 | Finite element structure analysis

Homogenization of stresses in bone can lead to evolutionary beneficial lightweight structures (Klenner, Witzel, Paris, & Distler, 2015). Such a loading regime is established by agonistically and antagonistically acting tension chords which can be either passive (ligaments) or active (muscles; Witzel & Preuschoft, 2005; Rayfield, 2007; Sverdlova & Witzel, 2010; Curtis, Witzel, Fitton, O'Higgins, & Fagan, 2011; Witzel, Mannhardt, Goessling, Micheli, & Preuschoft, 2011; Klenner, Witzel, Paris, & Distler 2015; Gilbert, Snively, & Cotton, 2016; Felsenthal & Zelzer, 2017). Because muscle forces are constantly changing during the flipper beat cycle of sea turtles, two load cases (Witzel & Preuschoft, 2005), that

is, the upstroke and downstroke of the foreflipper, were analyzed. The resulting functional loading is calculated by superposition of the loading conditions of all load cases (Carter, Orr, & Fyhrie, 1989). Functional loading of long bones leads to the development of bone curvature (Lanyon, 1980) which minimizes bending (McCabe, Henderson, Pantinople, Richards, & Milne, 2017; Milne, 2016). Long-term bending strains are reduced by bone remodeling (Lanyon, 1980). Computational simulations of the development of a human phalanx under axial compression and torsion correctly predicted its outer and inner bony structure (Lipphaus & Witzel, 2018). Muscle forces were calculated for a human femur model by minimization but not complete elimination of bending strain (Lutz et al., 2016). The model of Lutz et al. (2016) was validated by a finite element (FE) model, electromyography (EMG), and hip reaction force calculations which were computed and compared to data obtained from in vivo experiments by Bergmann et al. (2001).

Nonetheless, in vivo strains in vertebrate long bones indicate a more complex loading regime which includes bending, torsion, and axial compression (Biewener & Dial, 1995; Blob & Biewener, 1999; Butcher & Blob, 2008; Butcher, Espinoza, Cirilo, & Blob, 2008; Carrano, 1998; Lieberman, Polk, & Demes, 2004; Main & Biewener, 2004; Main & Biewener, 2007; Sheffield, Butcher, Shugart, Gander, & Blob, 2011; Young & Blob, 2015; Young, Wienands, Wilburn, & Blob, 2017). Long bones of vertebrates, including Testudines, are either loaded by bending alternatingly or to a relatively large extend by compressive stresses and to a significantly lower degree by tensile stresses (Biewener & Dial, 1995; Blob & Biewener, 1999; Butcher et al., 2008; Butcher & Blob, 2008; Lieberman et al., 2004; Main & Biewener, 2004; Sheffield et al., 2011). However, if the recorded load cases were superposed, their superposition would show a more homogenous stress distribution and predominantly compressive stresses as the generally lower tensile stresses would be cancelled out. In turtles that walk on land, high torsional loads were found in the long bones (Butcher et al., 2008; Butcher & Blob, 2008). Considerable torsional loads were reported for archosaurs (Biewener & Dial, 1995; Blob & Biewener, 1999; Carrano, 1998; Main & Biewener, 2007), lepidosaurs (Blob & Biewener, 1999; Sheffield et al., 2011), but less so in mammals (e.g., Main & Biewener, 2004). The shift from the terrestrial to the aquatic habitat in Testudines is accompanied by a significant reduction of torsional loading. This could be the reason for the evolution of limb bone shapes in highly aquatic turtles species that differ from the common tubular form observed in terrestrial Tetrapoda, which are well adapted for shear strains (Blob, Mayerl, Rivera, Rivera, & Young, 2016; Young et al., 2017; Young & Blob, 2015).

The aim of this study is to conduct finite element structure analysis (FESA) on a sea turtle humerus for two load cases based on the criterion of bending minimization. The analysis was supported by dissection of sea turtle humerus musculature. Muscle functions were determined and agonistic and antagonistic muscles were grouped. Muscle forces were calculated for the foreflipper downstroke and upstroke. The results support observations that during underwater flight of sea turtles, the foreflipper downstroke contributes more to propulsion than the upstroke. FESA of this cheloniid humerus supports the importance of bending minimization for lightweight bony structures (Curtis et al., 2011; Klenner et al., 2015; Sverdlova & Witzel, 2010; Witzel et al., 2011; Witzel & Preuschoft, 2005).

2 | MATERIALS AND METHODS

2.1 | Dissection of *Caretta caretta* humerus musculature

At the Stazione Zoologica Anton Dohrn of Naples (SZN), Italy, in the dedicated marine turtle research center, a subadult Mediterranean female *Caretta caretta* was dissected. Its carapace length as measured over the curve was 66.6 cm and a body mass of 33.38 kg. The turtle had been caught accidentally by a bottom-trawler and was brought to the SZN for rescue. However, the turtle died within 24 hr of its capture and was then frozen for later autopsy. The specimen was in good health as suggested by thick fat pads found during dissection. The main focus of the dissection of the *Caretta* specimen was the locomotory musculature of the foreflipper, especially those muscles that insert into, originate from, or span the humerus. Identification of these muscles was based on Walker (1973) and Wyneken (2001). Flexors and extensors were mainly identified by comparison with Walker (1973) (figure 17A and B, p. 51). Myological terminology is based on Walker (1973). For positional terms, we follow Romer (1976) in the usage of anterior versus posterior, ventral versus dorsal, and proximal versus distal, although these orientations do not necessarily correlate with humerus orientation during the movement cycle (see Davenport et al., 1984; Rivera et al., 2011 and Rivera et al., 2013 for description of the flipper beat cycle).

2.2 | Lines of action

The cheloniid specimen used for derivation of lines of action (LOA) is a *Chelonia mydas* (ZFMK 70222) from the Zoologisches Forschungsmuseum Alexander Koenig,
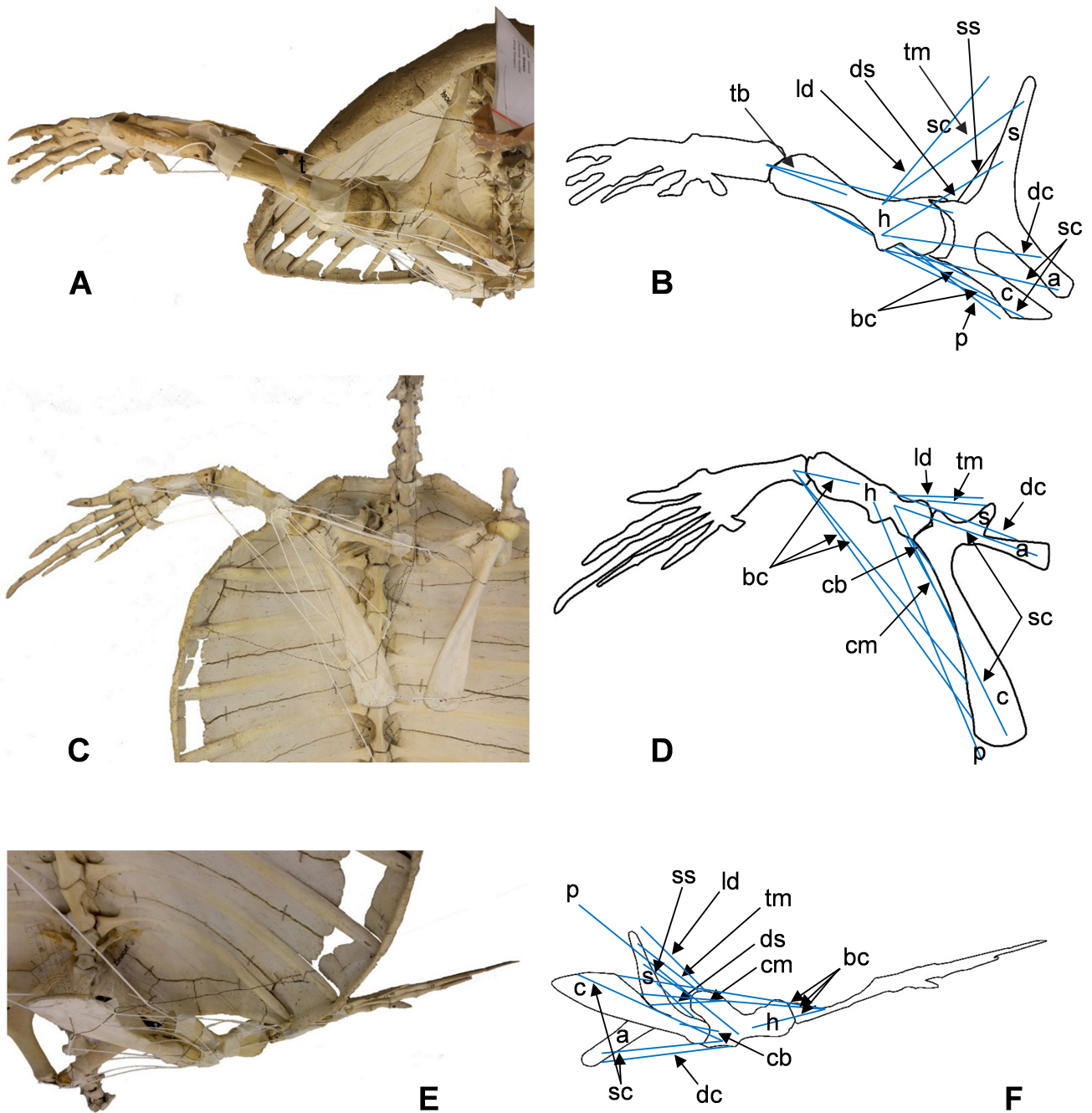
FIGURE 2 Lines of action (white threads/blue lines) of proximal humerus musculature of *Chelonia mydas* ZFMK 70222. Plastron removed. Note how all threads run in a fan shape from their humeral insertions towards the pectoral girdle. (b, d, f) contour drawings of (a, c, e). (a, b) anterior, (c, d) ventral, and (e, f) posteroventral view. a, acromion; bc, m. biceps complex (i.e., bi, brachialis inferior; bs, biceps superficialis; bp, biceps profundus); c, coracoid; cb, m. coracobrachialis brevis; cm, m. coracobrachialis magnus; dc, m. deltoideus clavicularis; ds, m. deltoideus scapularis; h, humerus; ld/tm, m. latissimus dorsi; s, scapula; tm, m. teres major; p, m. pectoralis; sc, m. supracoracoideus; ss, m. subscapularis; tb, m. triceps brachii

Bonn, Germany (Figure 2). It hat a curved carapace length of 107.7 cm. Lines of action are the connection between origin and insertion of a muscle in a straight line. They were obtained for each muscle inserting into, originating from, or spanning the humerus by clamping threads with tape onto the pectoral limb of ZFMK 70222.

For muscles that originate or insert on large areas, usually, the extreme points for attaching the threads were chosen, for example, for m. pectoralis (Figure 2). Two-bellied muscles were represented by two threads to show their main directions, although only the resultant vector was entered in the FE models. LOA were recorded in
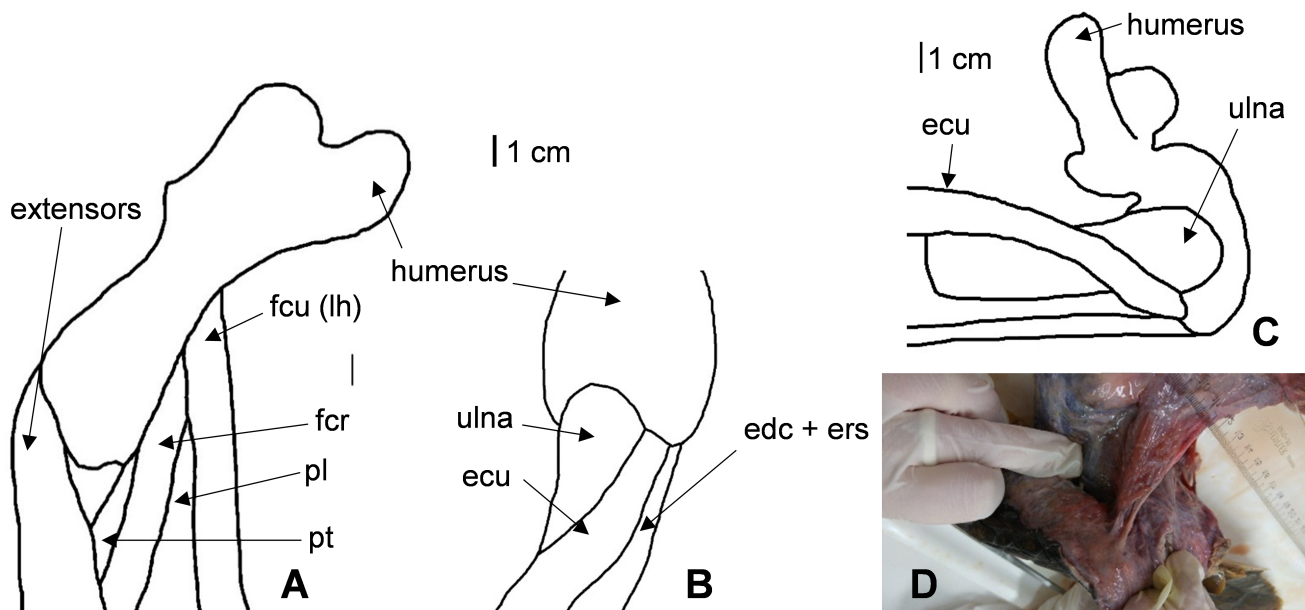
FIGURE 3 Dissection of right foreflipper of *Caretta caretta*. (a–c) Tracings from photographs taken during dissection. (a) Ventral view, note the strong bend of the humerus in relation to radius/ulna. (b) Dorsal view, ecu and ers + edc are "unwrapped". The straight articulation of humerus and radius/ulna is an artifact of muscle removal (compare to (a)). (c) This position equates to a flipper that is held at approximately body midline. Note how ecu wraps around the radius. The previously removed ers + edc wrapped only slightly around the radius, running toward the distal end of radius/ulna when the flipper is held in a neutral position. (d) fcu is inseparable from the dermis at the level of the pisiform. ecu, m. extensor carpi ulnaris; ers + edc, m. extensor radialis superficialis + m. extensor digitorum communis; fcr, m. flexor carpi radialis; fcu (lh), m. flexor carpi ulnaris lateral head; pl, palmaris longus; pt, m. pronator teres; tr, m. tractor radii

photographs. Photos of LOA were edited in Photoshop CS4. These photos provided the basis for sketches of the humerus and all its attaching muscles in form of LOA drawings. These were then implemented into the FE model (Figures 2a,c,e and 4a,e).

The plastron of ZFMK 70222 was removed because carapace and plastron largely covered the studied area. However, it was still not possible to photograph muscle attachments in standardized views because the carapace covers the pectoral girdle as well as the proximal half of the humerus in dorsal view. Therefore, views were chosen in a way that all muscles were visible from at least two different points of view and that as many muscles as possible were visible.

From the geometrical arrangement of lines of action, muscle functions and agonistic and antagonistic relationships were deduced (Tables 1 and 2). The terminology used below follows Rivera et al. (2011) who use protraction versus retraction and elevation versus depression to describe the movement directions of the *Caretta caretta* humerus. This terminology suits the concept of underwater flight best.

Muscle functions were derived for FESA solely by their geometrical arrangement. Muscle functions derived from electromyography (m. latissimus dorsi/teres major, m. triceps, m. pectoralis, m. coracobrachialis, m. deltoideus; Table 1) by Rivera et al. (2011) did not influence the

functional assessment at this point. However, discrepancies between the two methodically different data sets will be discussed in the relevant section.

2.3 | FE model generation and FESA load cases

The micro-CT scans were done at the Division of Paleontology at the Institute of Geosciences of the University of Bonn with a v|tome|x S240 scanner manufactured by GE phoenix|X-ray (Wunstorf, Germany). A total of 600 images with an exposure time of 667 ms and an average of four were recorded for the scan. Voxel size was 236.4 μm, the voltage was set to 80 mV and the current was set to 80 μA. The image stacks for the volume model were generated by the software VG Studio Max from the rotational X-ray images.

The image stack of humerus cross-sections in the x–y plane and z-direction generated from the micro-CT scans were imported into Simpleware ScanIP 5.1. By selecting a grey scale interval that includes cortex and spongiosa, but not their surroundings, the bony structure was segmented out in all images of the stack and used to generate the FE model of the bone (Figure 4a,e). Next, the volumetric model was meshed and then exported to
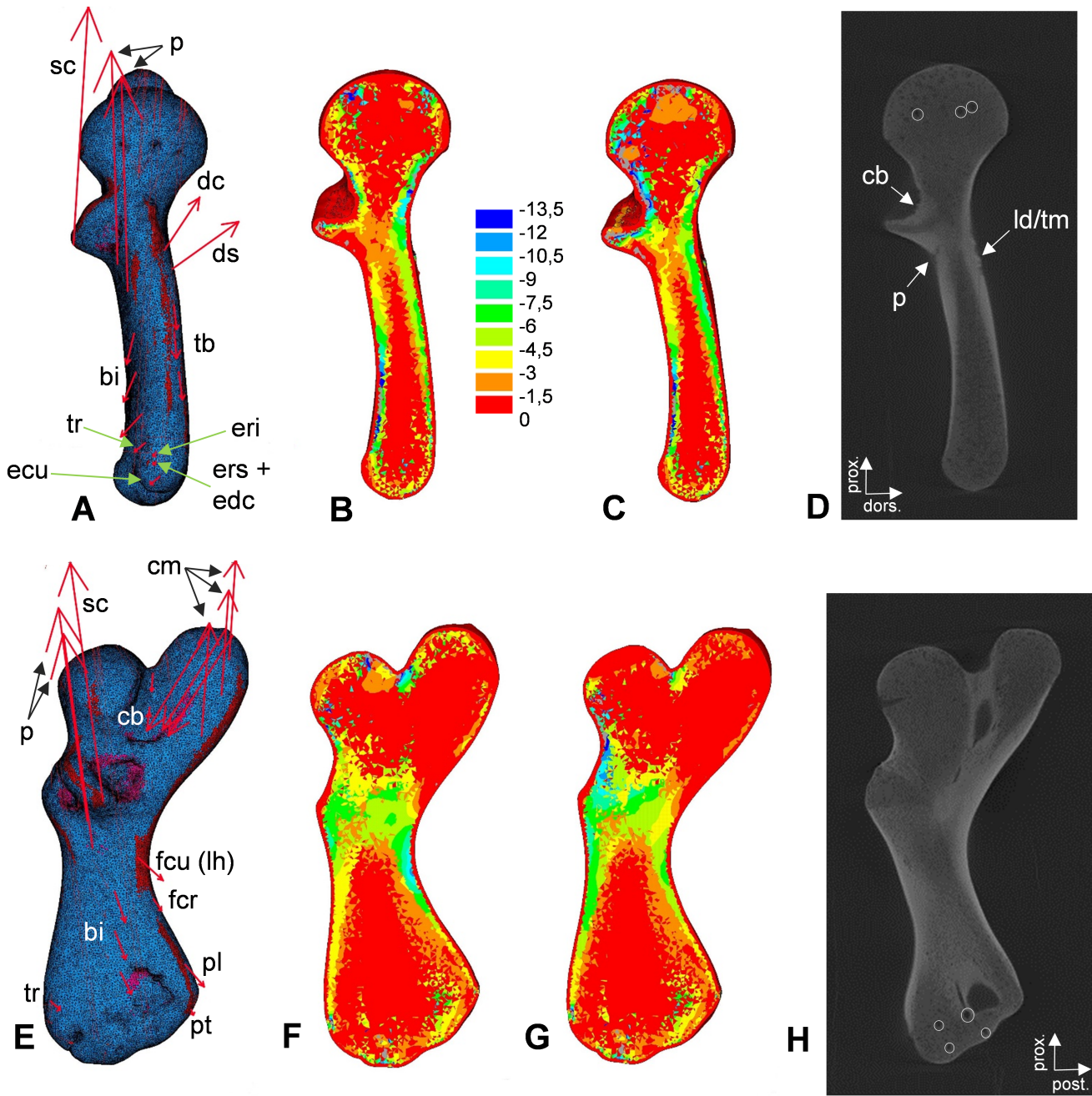
FIGURE 4 FESA of the right humerus of *Chelonia mydas* ZFMK 70222. (a, e) volume model with force vectors entered in (A) anterior view and (E) ventral view. (b, c, f, g) compressive stress distribution; (b and f) load case downstroke, (c and g) load case upstroke, (b and c) in anteroposterior view and (g and f) in dorsoventral view. (d, h) micro-CT slices in (d) anteroposterior view and (h) dorsoventral view. The color spectrum codes the compressive stress in MPa. Note how well areas of higher compressive stress (green and blue color spectrum) and lower compressive stress (yellow to red color spectrum; b, c, f, g) correspond with areas of compact bone (denser, or lighter appearing areas) and spongy bone (less dense, or darker appearing areas) in the micro-CT slices (b and c). White circles indicate artifacts from skeleton mounting (drill holes). bi, brachialis inferior; cb, m. coracobrachialis brevis; cm, m. coracobrachialis magnus; dc, m. deltoideus clavicularis; ds, m. deltoideus scapularis; ecu, m. extensor carpi ulnaris; eri, m. extensor radialis intermedius; ers + edc, m. extensor radialis superficialis + m. extensor digitorum communis; fcr, m. flexor carpi radialis; fcu (lh), m. flexor carpi ulnaris; ld/tm, m. latissimus dorsi/teres major; p, m. pectoralis; pl, m. palmaris longus; pt, m. pronator teres; sc, m. supracoracoideus; tb, m. triceps brachii; tr, m. tractor radii

ANSYS 16.0 (ANSYS Inc., Canonsburg, PA). Then, the volumetric model was scaled to the dimensions measured on the actual humerus, since micro-CT images are virtually composed slices. The FE model of the humerus was modeled using the element type "solid 185", which is tetrahedral and has eight nodes. The articulation surfaces

TABLE 1 Functions of Cheloniidae humerus musculature

Muscle	Function after Walker (1973)	Function after Wyneken (2001)	Function after Wyneken (2003)	Function after Rivera et al. (2011)	Own interpretation
m. latissimus dorsi/ m. teres major	Humeral abduction, less protraction	Humeral abduction, less protraction	Humeral abduction, less protraction	Elevator and protractor of humerus	Elevation, protraction
m. deltoideus clavicularis	Humeral abduction and protraction	Humeral protraction and abduction	Humeral abduction, less protraction	Constrains humerus retraction during downstroke	Depression, protraction
m. deltoideus scapularis					Elevation, protraction
m. subscapularis	Humeral abduction, protractor	Humeral protractor	Humeral protractor	–	Elevation, retraction
m. triceps brachii (triceps superficialis)	Flexion of antebrachium, humeral protraction and abduction	Humeral adduction; flipper twisting along its long axis, antebrachial abduction	Humeral adduction	Extends elbow	Elbow extension, diaphyseal compression
m. pectoralis	Humeral retraction and adduction	Humeral retraction and adduction	–	Humeral depression and retraction	Depression, retraction
m. supracoracoideus	Humeral retraction and adduction, humeral protraction by anterior fibres	Posterior portion: Humeral protraction and abduction; anterior portion: Humeral adduction and retraction	–	–	Posterior portions: Depression, retraction Anterior portions: Depression, protraction
m. coracobrachialis magnus	Humeral retraction, less abduction	Humeral retraction	–	Humeral depression and retraction	Depression, retraction
m. coracobrachialis brevis	Humeral retraction, adduction	–	–		Depression, retraction
m. biceps superficialis	Humeral retraction and antebrachial flexion	Humeral retraction	Controls flipper twist/rotation	–	Elbow flexion, diaphyseal compression, retraction
m. biceps profundus		Humeral retraction, antebrachial flexion	Humeral retraction, antebrachial flexion	–	
m. brachialis inferior		–	–	–	Flexion
m. flexor carpi ulnaris	Flexes antebrachium and Manus	–	–	–	Flexes antebrachium and Manus and rotates flipper
m. flexor carpi radialis	Antebrachial flexor	–	–	–	Antebrachial flexor and rotates flipper
m. palmaris longus	Flexes antebrachium, Manus and digits	–	–	–	Flexes antebrachium, Manus and digits
m. tractor radii	Antebrachial extensor	–	–	–	Antebrachial flexor
m. extensor carpi ulnaris	Antebrachial extensor	–	–	–	Antebrachial extensor and rotates flipper
m. pronator teres	Pronator of lower arm	–	–	–	Antebrachial flexor
m. extensor digitorum communis + m.	Extends Manus	–	–	–	Extends antebrachium,

(Continues)

T A B L E 1 (Continued)

Muscle	Function after Walker (1973)	Function after Wyneken (2001)	Function after Wyneken (2003)	Function after Rivera et al. (2011)	Own interpretation
extensor radialis superficialis					Manus, and rotates flipper
m. extensor radialis intermedius	Antebrachial extensor	–	–	–	Antebrachial extensor

Note: –, no muscle function deduced by the respective author.

T A B L E 2 Agonists and antagonists of the foreflipper of *Chelonia mydas*

Agonists	Antagonists
m. latissimus dorsi/m. teres major (elevation, protraction)	m. pectoralis (depression, retraction), m. supracoracoideus (posterior portions) (depression, retraction)
m. subscapularis (elevation, retraction), m. biceps (retraction)	m. deltoideus clavicularis (depression, protraction), anterior portions of m. supracoracoideus (depression, protraction)
m. deltoideus scapularis ([elevation] protraction)	m. coracobrachialis magnus, m. coracobrachialis brevis ([depression] retraction)
m. triceps (elbow extension and diaphyseal compression)	m. biceps (elbow flexion and diaphyseal compression)
m. triceps humeral head (elbow extension)	m. brachialis inferior (elbow flexion)
m. flexor carpi ulnaris (lateral and medial head) (rotates posterior edge down/anterior edge up)	m. extensor carpi ulnaris and m. flexor carpi radialis (rotate anterior flipper edge down)
m. flexor carpi ulnaris (lateral and medial head) (rotates posterior edge down/anterior edge up)	m. extensor radialis superficialis + m. extensor digitorum communis (rotate anterior flipper edge down)
m. extensor digitorum communis + m. extensor radialis superficialis (extension of lower arm)	m. palmaris longus (flexion of lower arm and digits)
m. extensor carpi ulnaris (extension of lower arm)	m. flexor carpi radialis (lower arm flexion, rotates flipper leading edge down)
m. extensor radialis intermedius (extension)	m. tractor radii (flexion), m. pronator teres (flexion), m. flexor carpi ulnaris (flexion)

of the humeral head were constrained by bearings, that is, the humeral head was immobilized. The FE model consists of 374,768 tetrahedral elements and 84,172 nodes. Both cortical bone and spongy bone were modeled with a Poisson's ratio of 0.3 (Preuschoft & Witzel, 2005; Witzel & Preuschoft, 2005). Via greyscale selection, Young's moduli were assigned to different microstructures. The material properties of spongiosa and cortex do not suddenly change. Their transition is gradually from lower to higher Young's moduli from the center toward the periphery of the bone. Therefore, the bone cortex was subdivided into areas with two different Young's moduli of 17,500 MPa and 8,000 MPa. The spongy bone was modeled with a Young's modulus of 410 MPa. Values for Young's moduli are based on Sverdlova and Witzel (2010).

Myologic characteristics, that is, origin, insertion, line of action, muscle wrapping (Figure 3c), were transferred into LOA drawings of the humerus in anterior, posterior, dorsal, and ventral views and then entered as force vectors into the FE model (Figure 4a,e). Vector origins in the FE model represent insertions and origins of muscles on humerus (Figure 1), vector directions are equal to the LOA (Figure 2) of the respective muscles, and vector sizes illustrate muscle force (Table 3). Some muscles with relatively large attachment areas on the humerus, that is, m. subscapularis, humeral head of m. triceps brachii, m. brachialis inferior, and m. coracobrachialis magnus, although they are represented by one LOA, were subdivided into several compartments. This means, that these muscles are not represented by one vector yielding the total force of the respective muscle, but by several smaller vectors that sum up to its total muscle force. These subdivisions were undertaken to obtain a more homogenous compressive stress distribution. Two-joint muscles, that is, m. triceps brachii and m. biceps brachii, span the humerus as they originate from the pectoral girdle and insert into the radius or the ulna. Muscle forces of m. triceps brachii and m. biceps brachii influence the

humerus FESA only indirectly. These muscles are represented by the resultant vectors acting on the distal humerus. They add to the counterforce which is applied to the humeral epicondyles by radius and ulna. The counterforce resulted from the axial components of the force vectors and the propulsive force. Although hydrodynamic forces have been calculated using computational fluid dynamics (CFD), complex movement and muscle activation make it impossible to define an average joint force. Therefore, the area of the joint was measured in the computational model to be 1,657 mm^2. Values of average physiological loads of cartilage are 1–2 MPa (Ateshian & Hung, 2006; Harris et al., 2012). The resulting counterforce was calculated using the joint area and an average contact pressure of 1.5 MPa. Vectors of muscles wrapping around bone are represented by split-up vectors with different directions. This is necessary because ANSYS is not able to simulate stresses generated by curved lines. Therefore, the muscle wrapping is broken down into several smaller (straight) vectors to trace the curved muscle.

As the loading regime changes during a limb cycle, two load cases (Figure 4b,c,f,g; Witzel & Preuschoft, 2005), downstroke and upstroke, that is, humeral elevation and depression were computed. We defined the following flipper position for downstroke and upstroke: The flipper trailing edge is angled at 90° to the cheloniid body length axis (through the midline; compare to Rivera et al., 2011, figure 1a) and where it is at the same height of the glenoid in lateral view (corresponding approximately to Davenport et al., 1984 figure 7, p. 455, interval 3 and 12). The long axis of the humerus is approximately angled at 45° to the body length axis (as derived from Rivera et al., 2011, figure 1, p. 3316).

Computing FESA of the two load cases is only possible if muscles are considered as pairs of agonists and antagonists (Table 2; Jenkins & Goslow, 1983; Sverdlova & Witzel, 2010; Witzel et al., 2011). During the downstroke, the agonists power depression and retraction of the humerus and flexion of the flipper at the elbow at high force levels. The opposing antagonists keep this movement controllable by exerting lower levels of force. Humeral elevators and protractors and elbow extensors become the agonistic muscles that enable the flipper upstroke which has a high force output at this part of the cycle. The antagonists, that is, the agonists from the downstroke, are now working at lower force levels and help to control the movements. At no point in the flipper beat cycle do all muscles work with maximum force at the same time. During normal swimming behavior, maximum muscle forces are likely not reached. High muscle forces are expected for the agonists of the downstroke and upstroke, while considerably lower muscle forces are expected for the antagonists. Muscle forces were determined in iterative steps (Table 3).

Humerus maximum muscle forces for the dissected *Caretta caretta* specimen were approximated. This was done by measuring muscle architectural details, presuming all muscles would be parallel-fibred, and calculating the cross-sectional areas of each muscle by employing the established formula for deriving muscle forces from the physiological cross-sectional areas (Alexander & Vernon, 1975; Anapol & Barry, 1996; Azizi, Brainerd, & Roberts, 2008; Gans, 1982; Narici, Landoni, & Minetti, 1992; Powell, Roy, Kanim, Bello, & Edgerton, 1984; Sacks & Roy, 1982). Then maximum muscle forces were calculated following, for example, Medler (2002) and (Gröning et al., 2013). Nevertheless, these approximated muscle forces provided us only with relative maximum force levels. This is because the FE model was built from a *Chelonia mydas* humerus of unknown ontogenetic stage (beyond early juvenile), and interspecific and intraspecific muscle (force) scaling relationships have not been established for extant sea turtle taxa.

Therefore, in a first run of the model, muscle forces were simply assumed based on relative muscle force levels gained from the *Caretta caretta* dissection, and the compressive stress distribution was computed. Then muscle forces were adjusted in such a way that bending moments in the model were minimized and compressive stresses were maximized, and the FESA was rerun. These steps were repeated until a homogenous compressive stress distribution was obtained for the whole bone volume (Sverdlova & Witzel, 2010; Witzel & Preuschoft, 2005).

3 | RESULTS

3.1 | Muscle functions and myology of the cheloniid foreflipper based on dissection and lines of action

The threads attached to the skeleton of ZFMK 70222 revealed the following lines of action (LOA; Figure 2) and muscle functions (Table 1): m. latissimus dorsi/teres major, m. deltoideus scapularis, and m. subscapularis elevate the humerus, whereas m. deltoideus clavicularis, m. pectoralis, m. supracoracoideus, m. coracobrachialis magnus, and m. coracobrachialis brevis depress it. Humeral protraction is provided by m. latissimus dorsi/teres major, m. deltoideus clavicularis, m. deltoideus scapularis, and the anterior portions of m. supracoracoideus. Contrastingly, retraction is provided by m. subscapularis, m. pectoralis, posterior portions of m. supracoracoideus, m. coracobrachialis magnus, m. coracobrachialis brevis, and the m. biceps complex. The antebrachium is flexed by m. flexor carpi ulnaris, m. flexor

carpi radialis, m. palmaris longus, m. tractor radii, m. pronator teres, and the m. biceps complex (Figure 3c,d). The manus is flexed by m. flexor carpi ulnaris and m. palmaris longus. The latter flexes the digits, too. Extension of the antebrachium is performed by m. extensor carpi ulnaris, m. extensor radialis superficialis + extensor digitorum communis (both muscles are fused in cheloniids according to Walker (1973)), extensor radialis intermedius, and m. triceps brachii, whereas m. extensor radialis superficialis + extensor digitorum communis also extend the manus. The leading edge of the flipper is rotated downwards by m. flexor carpi radialis and m. extensor carpi ulnaris and possibly also by m. extensor radialis superficialis + extensor digitorum communis (Figure 3a,b,e,f). The antagonist for this function is m. flexor carpi ulnaris.

A common tendon is shared by m. latissimus dorsi/teres major which inserts into a large scar on the dorsal humerus shaft (Figure 1). The two deltoid muscles, m. deltoideus scapularis and m. deltoideus clavicularis, converge into a large tendon. The part that m. deltoideus clavicularis mostly contributes to inserts anteriorly into the proximodistally extending leg of the v-shaped deltopectoral crest (Figure 1). The part of the tendon that m. deltoideus scapularis contributes to mostly, attaches dorsally in between the m. deltoideus clavicularis and m. latissimus dorsi/teres major areas onto a smooth, unscarred bone surface. The m. pectoralis tendon inserts into the ventral humerus, distally to the v-shaped deltopectoral crest, at a large and deep muscle scar (Figure 1). The large common tendon of all four m. supracoracoideus muscle bellies inserts into the ventral leg of the v-shaped deltopectoral crest (Figure 1). The tendinous part of m. coracobrachialis magnus inserts into the proximal textured part of the medial process which is demarcated by a line. This line demarcates bone covered by periosteum and the fibrocartilagenous insertion. The rest of m. coracobrachialis magnus inserts by fleshy fibers, that is, by muscle fibers and not by a tendon, into the approximate half of the medial process posteroventrally and extends down to the shaft, leaving no osteological correlates (Figure 1). The main bulk of m. coracobrachialis brevis inserts by fleshy fibers into the intertubercular fossa distally and above the ventral branch of the v-shaped deltopectoral crest. Yet, this insertion area is associated with a relatively large and deep muscle scar in comparison to muscle size (Figure 1). Neither flexors nor extensors leave visible osteological correlates on the distal humerus. Musculus coracobrachialis magnus wraps around the medial process. Around the bony saddle, between the humeral head and medial process, m. coracobrachialis brevis is wrapped.

Furthermore, m. triceps brachii, m. extensor carpi ulnaris, m. extensor radialis superficialis + extensor digitorum communis, and m. extensor radialis intermedius are found to wrap around the distal humerus when the elbow is flexed (Figures 3 and 4a,e). Adjacent to the pisiform, m. flexor carpi ulnaris inserts into the dermis (Figure 3d). We were not able to identify m. extensor radialis intermedius and the tendinous scapular head of the m. triceps brachii. Accordingly, we had to rely on literature data for the FE model (Walker, 1973; Wyneken, 2001). The former muscle arises tendinously dorsally to the glenoid from the scapula and inserts in common with the humeral head. The latter originates from the radial epicondyle proximal to m. extensor radialis superficialis + extensor digitorum communis and distal to m. tractor radii, and it inserts dorsally into the radius along its whole length (Walker, 1973). Four muscle bellies of m. supracoracoideus (taking their origin from the coracoid, acromion, plastron and medial scapula, and acromiocoracoid ligament) were found.

3.2 | FESA of the *Chelonia mydas* humerus

Initial iterative steps of FESA left the medial process and the radial epicondyle unloaded by compressive stress. Under predictions of FESA, unloaded regions indicate either that there exists no bony material in the biological structure, or that the model is still flawed. The former can be excluded because the FE model was built from micro-CTs of a real bony structure, the latter was considered more likely. The medial process and the distal epicondyles were loaded by compressive stress in subsequent runs, when the muscle wrappings of the m. coracobrachialis magnus and m. coracobrachialis brevis around the medial process and the extensors wrapping around the radial condyle were added. Muscle wrapping imposes compressive force vectors on bony features mentioned above. In contrast, muscles that do not wrap around bony structures only impose tensile loading onto their attachment region, although they may contribute to load bone compressively across a joint. Muscle wrappings prove to be crucial for receiving realistic FESA results.

The micro-CT scans of the humerus show the hourglass shape of the compact cortex, being thickest in the center of growth at mid diaphysis and thinning out towards the proximal and distal epiphyses. Underneath the thin cortical joint caps lie cones of spongy bone. The FE model shows moderate to high compressive stress (-3.0 to -13.5 MPa) that corresponds well to the compact cortex (grey areas in the CT scan), whereas low compressive stresses (-1.5 to -3.0 MPa) correspond to spongy bone in the region of the humeral head and the proximal and distal epiphyses (Figure 4b–d,f–h). The bridge

TABLE 3 Muscle forces for *Chelonia mydas* humerus musculature

Muscle	Load case downstroke (N)	Load case upstroke (N)
m. latissimus dorsi + teres major	129	259
m. deltoideus clavicularis	365	182
m. deltoideus scapularis	91	181
m. subscapularis	437	873
m. triceps	77	77
m. pectoralis	1,210	605
m. supracoracoideus	1,100	414
m. coracobrachialis magnus	970	485
m. coracobrachialis brevis	22	11
m. biceps	294	294
m. brachialis	291	146
m. tractor radii	52	26
m. extensor radialis superficialis + m. extensor digitorum communis	32	65
m. extensor carpi ulnaris	11	22
m. extensor radialis intermedius	10	20
m. flexor carpi ulnaris (medial part)	22	11
m. flexor carpi ulnaris (lateral part)	87	43
m. palmaris longus	24	49
m. flexor carpi radialis	52	26
m. pronator teres	23	26

between the medial process and the humeral head displays a thicker covering of compact cortex than the adjacent areas. The FE model shows high compressive stresses, up to −13.5 MPa in this region (Figure 4b,c,f,g). The richness in detail with which bone microanatomical features could be redrawn by the FESA validate the accuracy of the musculoskeletal model build for the cheloniid humerus. Differences between the compressive stress distributions of the two load cases indicate subordinate tensile forces (Figure 4b,c,f,g).

During the downstroke load case, the agonistic muscles depress and retract the humerus. and the flexors flex the flipper at the elbow and rotate the leading edge downward. The antagonists with the opposing functions control the movement. During the upstroke load case, muscles that are responsible for humeral elevation and protraction, flipper extension at the elbow and flipper leading edge upward rotation become the agonists. For

the first time, muscle forces imposing a compressive stress regime for cheloniid humerus musculature was derived experimentally by FESA. An agonistic muscle operates with about twice the force with which it operates as an antagonistic muscle. For example, when m. coracobrachialis magnus functions as an agonist in flipper depression and retraction during the downstroke, it develops a muscle force of 970 N. Contrastingly, it only operates with half that force, 485 N (Tables 2 and 3), when it functions as an antagonist. During the downstroke load case, m. pectoralis is the strongest muscle (1,210 N) followed closely by m. supracoracoideus (1,100 N). The muscle with the highest muscle force during the upstroke is m. subscapularis (873 N). The forces of the muscles inserting into the proximal half of the humerus are substantially higher than those originating from the distal half (Table 3), despite the counterforce induced by radius and ulna during swimming which had been added. Forces of those muscles inserting proximally into the humerus range from 91 to 1,210 N. Contrastingly, muscle forces of extensors and flexors arising from the distal humerus range from around 11 to 87 N.

4 | DISCUSSION

In comparison to *Pseudemys scripta elegans* muscle attachments described by Walker (1973) (figure 6, p. 16), muscles inserting into the humerus (m. coracobrachialis magnus, m. coracobrachialis brevis, m. subscapularis, m. deltoideus scapularis, m. deltoideus clavicularis, m. supracoracoideus, m. pectoralis, m. latissimus dorsi/ teres major) are relocated distally toward the shaft in *Caretta caretta* (Figure 1; compare to Walker (1973), figure 6, p. 16). The anterior edge of the cheloniid humerus is rather straight, and the extensors (except for m. tractor radii) of Cheloniidae are placed distally, close to the radial capitellum and close to the elbow joint capsule, as seen in *Pseudemys* Walker (1973) (Figure 1). Posteriorly the humerus of Cheloniidae is markedly curved and distally expanded (Figure 1). In *Caretta caretta*, the flexor origin areas are shifted proximally by up to half of the humerus length, and they are markedly larger than the extensors (Figure 1). Possibly, the proximal shift of flexor attachments onto the humeral shaft induces the humerus' posterior curvature and provides a more efficient moment arm. The difference in extensor and flexor size is consistent with the observation by Davenport et al. (1984) that the downstroke contributes more to propulsion than the upstroke.

Interpretations of muscle functions (Table 1) mostly corroborate the results of Walker (1973), Wyneken (2001), Wyneken (2003), and Rivera et al. (2011) for the pectoral

musculature and those of Walker (1973) for the limb extensors and flexors. Electromyographically derived functions for m. latissimus dorsi/teres major, m. pectoralis, coracobrachialis, and m. triceps brachii by Rivera et al. (2011) were corroborated in this study. For m. deltoideus, Rivera et al. (2011) did not distinguish between the scapular and the clavicular head and did not state which head was implanted with an electrode. M. deltoideus was found to be active as an antagonist to the retractional and depressional function of m. pectoralis during the downstroke (Rivera et al., 2011). This could possibly indicate that the EMG study obtained data for the clavicular head of m. deltoideus, and that more refined EMG data for m. deltoideus scapularis would show the expected activational pattern during humeral protraction and elevation. The largest differences between the results presented here and those of other authors were found in the function of the scapular head of the m. triceps brachii and the coracoidal heads of the m. biceps complex, and in m. coracobrachialis magnus, m. coracobrachialis brevis, m. extensor radialis superficialis + extensor digitorum communis, m. extensor carpi ulnaris, m. flexor carpi radialis, and m. flexor carpi ulnaris. While the coracoidal heads of the m. biceps complex may add to retraction power, the moment arm of m. triceps brachii is inappropriate for an elevational component.

Our finite element modeling showed that it was impossible to load the humeral diaphysis by compression without including muscle forces of the two-joint muscles (m. triceps brachii, m. biceps complex). While the proximal pectoral musculature pulls the humeral head into the glenoid, the distal extensors and flexors likewise pull radius and ulna into the humeral epiphyses. The 2 two-joint muscles (m. triceps brachii, m. biceps complex) are the only muscles that compress the region of the humeral diaphysis. The tension-cording of the two-joint muscles assists the bending minimized sea turtle humerus by altering the joint force. Therefore, changes in the direction of the joint force and removal of the main pectoral antagonistic muscles during downstroke (m. latissimus dorsi/teres major, m. subscapularis, m. triceps) lead to bending in the FE-model of the humerus (Figure 5; compare to Figure 4b,c,f,g).

Contrastingly to the diaphysis, the proximal epiphysis is functionally loaded by compression by all other pectoral muscles. The distal epiphysis is compressed by the extensors and flexors that originate from the distal humerus. Thus, dissection showed that m. extensor radialis superficialis + extensor digitorum communis, m. extensor carpi ulnaris, and m. flexor carpi radialis have the additional function of jointly rotating the leading edge of the cheloniid flipper ventrally. These are the muscles that diagonally cross the antebrachium. Musculus flexor carpi
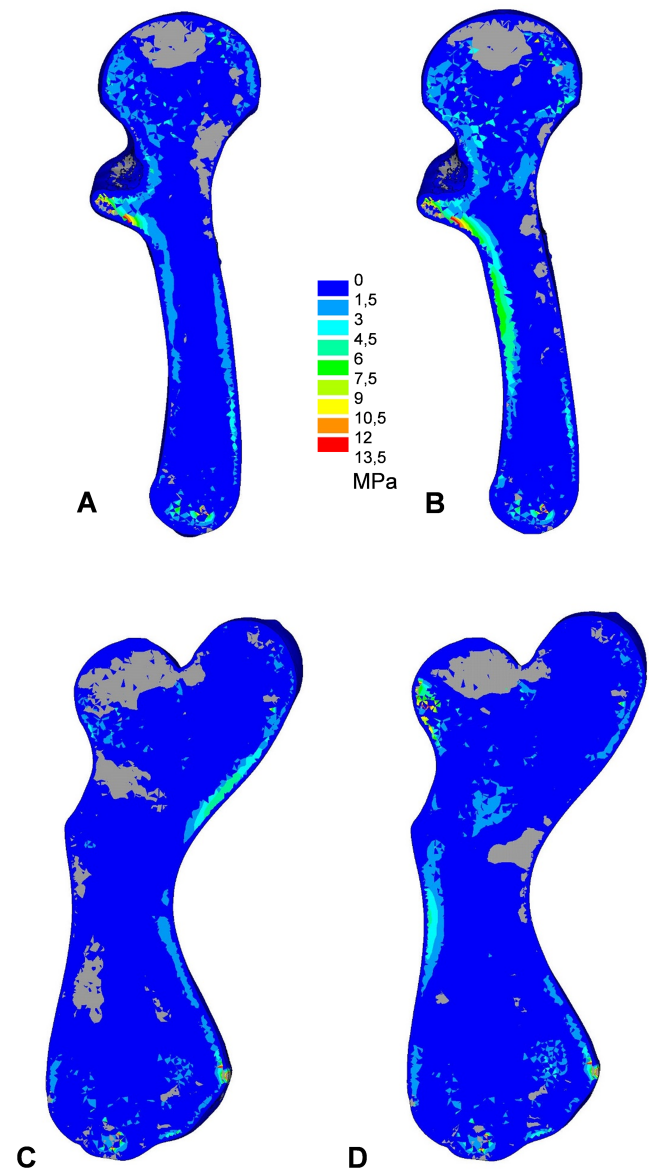

FIGURE 5 FESA of the right humerus of *Chelonia mydas* ZFMK 70222 shows the tensile stress distribution during downstroke with active tension-cording (i.e., active antagonistic muscles) in (a) anteroposterior view and (c) dorsoventral view and without active tension-cording in (b) anteroposterior view and (d) dorsoventral view. Panels (a) and (c) display low tensile stress and therefore minimized bending. Panel (b) shows significant tensile stresses and therefore bending. Panel (d) displays no significant bending, as there is a forward thrust force in the same direction in both load cases

ulnaris is the only muscle that appears to have an appropriate lever arm to rotate the leading edge of the flipper dorsally.

The EMG activity patterns obtained for five selected cheloniid muscles by Rivera et al. (2011) document their active contraction during the limb cycle. They did not find any activity in the potential antagonistic muscles.

During the passive stretching of a muscle, a significantly lower activity, the resting potential, should be expected. This appears to contradict our findings that antagonistic muscles are also active and develop muscle forces although, according to the EMG, they should seemingly be inactive. Muscles experience either a stretching–shortening or a shortening–stretching cycle during a movement (Rassier, MacIntosh, & Herzog, 1999). On the one hand, muscles that experience stretching, passively resist their stretching by intrinsic forces (e.g., Gordon, Huxley, & Julian, 1966). On the other hand, antagonistic muscles show detectable electric activation, just markedly lower than the agonistic muscles (Aagaard et al., 2000). Therefore, an EMG study that specifically investigates agonistic and antagonistic muscle activity in sea turtles could test the findings of this study. Strain gauges could give insights into the in vivo loading regime of cheloniid humeri during underwater flight. Maximum muscle force determination with the help of physiological cross-sectional areas of cheloniids that are of similar size as the *Chelonia mydas* in the current study could corroborate the magnitude of muscle forces calculated by FESA.

Many muscles were found to wrap around bony parts (medial process, bridge between medial process and humeral head, radial epicondyle): m. croacobrachialis magnus, m. coracobrachialis brevis, m. extensor radialis superficialis + extensor digitorum communis, m. extensor carpi ulnaris, m. extensor radialis intermedius, and m. triceps brachii. These muscles prove to be important because, without them, it would be impossible to load adjacent bony regions by compressive stresses and they would be solely loaded by tensile stresses (Figure 4a,e; Curtis, Kupczik, O'Higgins, Moazen, & Fagan, 2008).

Initial versions of the model resulted in, for example, highly loaded spongy areas, insufficiently loaded compact cortical regions, and even tensile stresses. After dissection of the *Caretta* specimen and numerous refinements of muscle forces and directions, the FE models (strength of compressive forces) and micro-CTs (degree of bone compactness; Figure 4b–d,f–h) match very well. Although Young's moduli were set manually in advance based on the greyscale values of the micro-CTs, this supports our hypotheses about LOA and muscle forces. For the upstroke, m. subscapularis produces the highest muscle force (792 N), whereas for the downstroke, m. pectoralis produces the highest muscle force (1,100 N; Table 3). This corroborates the observation by Davenport et al. (1984) that the downstroke contributes relatively more to propulsion than the upstroke. Future studies deriving muscle forces via physiological cross-sectional areas and elaborate EMG studies focusing on agonistic and antagonistic muscle relationships and strain gauges could validate our FESA results and further establish FESA is a noninvasive method for muscle force determination.

ORCID

Anna Krahl https://orcid.org/0000-0003-1806-2907

REFERENCES

Aagaard, P., Simonsen, E. B., Andersen, J. L., Magnusson, S. P., Bojsen-Moller, F., & Dyhre-Poulsen, P. (2000). Antagonist muscle coactivation during isokinetic knee extension. *Scandinavian Journal of Medicine & Science in Sports*, *10*, 58–67.

Abdala, V., Manzano, A. S., & Herrel, A. (2008). The distal forelimb musculature in aquatic and terrestrial turtles: Phylogeny or environmental constraints? *Journal of Anatomy*, *213*, 159–172.

Alexander, R. M., & Vernon, A. (1975). The dimensions of knee and ankle muscles and the forces they exert. *Journal of Human Movement Studies*, *1*, 115–123.

Anapol, F., & Barry, K. (1996). Fiber architecture of the extensors of the hindlimb in semiterrestrial and arboreal guenons. *American Journal of Physical Anthropology*, *99*, 429–447.

Ateshian, G. A., & Hung, C. T. (2006). Functional properties of native articular cartilage. In F. Guilak, D. L. Butler, S. A. Goldstein, & D. Mooney (Eds.), *Functional tissue engineering* (p. 48). New York, Berlin, Heidelberg: Springer.

Azizi, E., Brainerd, E. L., & Roberts, T. J. (2008). Variable gearing in pennate muscles. *Proceedings of the National Academy of Sciences of the United States of America*, *105*, 1745–1750.

Bergmann, G., Deuretzbacher, G., Heller, M., Graichen, F., Rohlmann, A., Strauss, J., & Duda, G. N. (2001). Hip contact forces and gait patterns from routine activities. *Journal of Biomechanics*, *34*, 859–871.

Biewener, A. A., & Dial, K. P. (1995). In vivo strain in the humerus of pigeons (*Cloumba livia*) during flight. *Journal of Morphology*, *225*, 61–65.

Blob, R. W., & Biewener, A. A. (1999). In vivo locomotor strain in the hindlimb bones of *Alligator mississpiensis* and *Iguana iguana*: Implications for the evolution of limb bone safety factor and non-sprawling limb posture. *The Journal of Experimental Biology*, *202*, 1023–1046.

Blob, R. W., Mayerl, C. J., Rivera, A. R. V., Rivera, G., & Young, V. K. H. (2016). "On the fence" versus "all in": Insights from turtles for the evolution of aquatic locomotor specializations and habitat transitions in tetrapod vertebrates. *Integrative and Comparative Biology*, *56*, 1310–1322.

Butcher, M. T., & Blob, R. W. (2008). Mechanics of limb bone loading during terrestrial locomotion in river Cooter turtles (*Pseudemys concinna*). *The Journal of Experimental Biology*, *211*, 1187–1202.

Butcher, M. T., Espinoza, N. R., Cirilo, S. R., & Blob, R. W. (2008). In vivo strains in the femur of river Cooter turtles (*Pseudemys concinna*) during terrestrial locomotion: Tests of force-platform models of loading mechanics. *The Journal of Experimental Biology*, *211*, 2397–2407.

Carrano, M. T. (1998). Locomotion in non-avian dinosaurs: Integrating data from hindlimb kinematics, in vivo strains, and bone morphology. *Paleobiology*, *24*, 450–469.

Carter, D. R., Orr, T. E., & Fyhrie, D. P. (1989). Relationships between loading history and femoral cancellous bone architecture. *Journal of Biomechanics*, *22*, 231–244.

Curtis, N., Kupczik, K., O'Higgins, P., Moazen, M., & Fagan, M. J. (2008). Predicting skull loading: Applying multibody dynamics analysis to a macaque skull. *The Anatomical Record*, *291*, 491–501.

Curtis, N., Witzel, U., Fitton, L., O'Higgins, P., & Fagan, M. J. (2011). The mechanical significance of the temporal fasciae in *Macaca fascicularis*: An investigation using finite element analysis. *The Anatomical Record*, *294*, 1178–1190.

Davenport, J., Munks, S. A., & Oxford, P. J. (1984). A comparison of the swimming of marine and freshwater turtles. *Proceedings of the Royal Society B: Biological Sciences*, *220*, 447–475.

Depecker, M., Berge, C., Penin, X., & Renous, S. (2006). Geometric morphometrics of the shoulder girdle in extant turtles (Chelonii). *Journal of Anatomy*, *208*, 35–45.

Felsenthal, N., & Zelzer, E. (2017). Mechanical regulation of musculoskeletal system development. *Development*, *144*, 4271–4283.

Francillon-Vieillot, H., de Buffrénil, V., Castanet, J., Géraudie, J., Meunier, F. J., Sire, J. Y., … de Ricqlès, A. (1990). Microstructure and mineralization of vertebrate skeletal tissues. In J. G. Carter (Ed.), *Skeletal biomineralization. Patterns, processes and evolutionary trends* (pp. 499–512). New York: Van Nostrand Reinhold.

Gans, C. (1982). Fibre architecture and muscle function. *Exercise and Sport Sciences Reviews*, *10*, 160–207.

Gilbert, N. M., Snively, E., & Cotton, J. R. (2016). The tarsometatarsus of the ostrich *Struthio camelus*: Anatomy, bone density, and structural mechanics. *PLoS One*, *11*, e0149708.

Gordon, A. M., Huxley, A. F., & Julian, F. J. (1966). The variation in isometric tension with sarcomere length in vertebrate muscle fibres. *The Journal of Physiology*, *184*, 170–192.

Gröning, F., Jones, M. E. H., Curtis, N., Herrel, A., O'Higgins, P., Evans, S. E., & Fagan, M. J. (2013). The importance of accurate muscle modelling for biomechanical analyses: A case study with a lizard skull. *Journal of the Royal Society Interface*, *10*, 1–10.

Harris, M. D., Anderson, A. E., Henak, C. R., Ellis, B. J., Peters, C. L., & Weiss, J. A. (2012). Finite element prediction of cartilage contact stresses in normal human hips. *Journal of Orthopaedic Research*, *30*, 1133–1139.

Hirayama, R. (1994). Phylogenetic systematics of chelonioid sea turtles. *Island Arc*, *3*, 270–284.

Jenkins, F. A., & Goslow, G. E. (1983). The functional anatomy of the shoulder of the savannah monitor lizard (*Varanus exanthematicus*). *Journal of Morphology*, *175*, 195–216.

Klenner, S., Witzel, U., Paris, F., & Distler, C. (2015). Structure and function of the septum nasi and the underlying tension chord in crocodylians. *Journal of Anatomy*, *228*, 113–124.

Lanyon, L. E. (1980). The influence of function on the development of bone curvature: An experimental study on the rat tibia. *Journal of Zoology*, *192*, 457–466.

Lieberman, D. E., Polk, J. D., & Demes, B. (2004). Predicting long bone loading from cross-sectional geometry. *American Journal of Physical Anthropology*, *123*, 156–171.

Lipphaus, A., & Witzel, U. (2018). Biomechanical study of the development of long bones: Finite element structure synthesis of the human second proximal phalanx under growth conditions. *The Anatomical Record*, *302*, 1389–1398.

Lutz, F., Mastel, R., Runge, M., Stief, F., Schmidt, A., Meurer, A., & Witte, H. (2016). Calculation of muscle forces during normal gait under consideration of femoral bending moments. *Medical Engineering & Physics*, *38*, 1008–1015.

Main, R. P., & Biewener, A. A. (2004). Ontogenetic patterns of limb loading, in vivo bone strains and growth in the goat radius. *The Journal of Experimental Biology*, *207*, 2577–2588.

Main, R. P., & Biewener, A. A. (2007). Skeletal strain patterns and growth in the emu hindlimb during ontogeny. *The Journal of Experimental Biology*, *210*, 2676–2690.

McCabe, K., Henderson, K., Pantinople, J., Richards, H. L., & Milne, N. (2017). Curvature reduces bending strains in the quokka femur. *PeerJ*, *5*, e3100.

Medler, S. (2002). Comparative trends in shortening velocity and force production in skeletal muscles. *The American Journal of Physiology*, *283*, 368–378.

Milne, N. (2016). Curved bones: An adaptation to habitual loading. *Journal of Theoretical Biology*, *407*, 18–24.

Narici, M. V., Landoni, L., & Minetti, A. E. (1992). Assessment of human knee extensor muscles stress from in vivo physiological cross-sectional area and strength measurements. *European Journal of Applied Physiology*, *65*, 438–444.

Pace, C. M., Blob, R. W., & Westneat, M. W. (2001). Comparative kinematics of the forelimb during swimming in red-eared slider (*Trachemys scripta*) and spiny softshell (*Apalone spinifera*) turtles. *The Journal of Experimental Biology*, *204*, 3261–3271.

Powell, P. L., Roy, R. R., Kanim, P., Bello, M. A., & Edgerton, V. R. (1984). Predictability of skeletal muscle tension from architectural determinations in Guinea pig hindlimbs. *Journal of Applied Physiology*, *57*, 1715–1721.

Preuschoft, H., & Witzel, U. (2005). Functional shape of the skull in vertebrates: Which forces determine skull morphology in lower

primates and ancestral synapsids? *The Anatomical Record*, *283*, 402–413.

Rassier, D. E., MacIntosh, B. R., & Herzog, W. (1999). Length dependence of active force production in skeletal muscle. *Journal of Applied Physiology*, *86*, 1445–1457.

Rayfield, E. J. (2007). Finite element analysis and understanding the biomechanics and evolution of living and fossil organisms. *Annual Review of Earth and Planetary Sciences*, *35*, 541–576.

Renous, S. (1995). The ontogeny of locomotion in marine turtles. In G. A. Llorente, A. Montori, X. Santos, & M. A. Carretero (Eds.), *Scienta Herpetologica* (pp. 112–119). Barcelona, Spain: Asociación Herpetológica Espanola.

Rivera, A. R. V., Rivera, G., & Blob, R. W. (2013). Forelimb kinematics during swimming in the pig-nosed turtle, *Carettochelys insculpta*, compared with other turtle taxa: Rowing versus flapping, convergence versus intermediacy. *The Journal of Experimental Biology*, *216*, 668–680.

Rivera, A. R. V., Wyneken, J., & Blob, R. W. (2011). Forelimb kinematics and motor patterns of swimming loggerhead sea turtles (*Caretta caretta*): Are motor patterns conserved in the evolution of new locomotor strategies? *The Journal of Experimental Biology*, *214*, 3314–3323.

Romer, A. S. (1976). *Osteology of the reptiles* (3rd ed.). Chicago, IL: University of Chicago Press.

Sacks, R. D., & Roy, R. R. (1982). Architecture of the hind limb muscles of cats: Functional significance. *Journal of Morphology*, *173*, 185–195.

Sheffield, K. M., Butcher, M. T., Shugart, S. K., Gander, J. C., & Blob, R. W. (2011). Locomotor loading mechanics in the hindlimbs of tegu lizards (*Tupinambis merianae*): Comparative and evolutionary implications. *The Journal of Experimental Biology*, *214*, 2616–2630.

Sverdlova, N. S., & Witzel, U. (2010). Principles of determination and verification of muscle forces in the human musculoskeletal system: Muscle forces to minimise bending stress. *Journal of Biomechanics*, *43*, 387–396.

Walker, J. A., & Westneat, M. W. (2000). Mechanical performance of aquatic rowing and flying. *Proceedings of the Royal Society B: Biological Sciences*, *267*, 1875–1881.

Walker, W. F. (1971). A structural and functional analysis of walking in the turtle, *Chrysemys picta marginata*. *Journal of Morphology*, *134*, 195–214.

Walker, W. F. (1973). The locomotor apparatus of Testudines. *Biology of Reptilia*, *4*, 1–100.

Witzel, U., Mannhardt, J., Goessling, R., Micheli, P., & Preuschoft, H. (2011). Finite element analyses and virtual syntheses of biological structures and their application to sauropod skulls. In N. Klein, K. Remes, C. T. Gee, & P. M. Sander (Eds.), *Biology of the Sauropod dinosaurs: Understanding the life of giants* (pp. 171–182). Bloomington, IN: Indiana University Press.

Witzel, U., & Preuschoft, H. (2005). Finite-element model construction for the virtual synthesis of the skulls in vertebrates: Case study of *Diplodocus*. *The Anatomical Record*, *283*, 391–401.

Wyneken, J. (1997). Sea turtle locomotion: Mechanisms, behavior, and energetics. In P. L. Lutz & J. A. Musick (Eds.), *The biology of sea turtles* (pp. 165–198). Boca Raton, FL: CRC Press.

Wyneken, J. (2001). *The Anatomy of Sea Turtles, NMFS-SEFSC-470*. Miami: NOAA Technical Memorandum.

Wyneken, J. (2003). The external morphology, musculoskeletal system, and neuro-anatomy of sea turtles. *The Biology of Sea Turtles*, *2*, 39–77.

Young, V. K. H., & Blob, R. W. (2015). Limb bone loading in swimming turtles: Changes in loading facilitate transitions from tubular to flipper-shaped limbs during aquatic invasions. *Biology Letters*, *11*, 20150110.

Young, V. K. H., Wienands, C. E., Wilburn, B. P., & Blob, R. W. (2017). Humeral loads during swimming and walking in turtles: Implications for morphological change during aquatic reinvasions. *The Journal of Experimental Biology*, *220*, 3873–3877.